

Silicon-plasmonic internal-photoemission detector for 40 Gbit/s data reception

S. MUEHLBRANDT,^{1,2,5} A. MELIKYAN,^{1,2} T. HARTER,^{1,2} K. KÖHNLE,^{1,2} A. MUSLIJA,¹ P. VINCZE,³ S. WOLF,² P. JAKOBS,¹ Y. FEDORYSHYN,⁴ W. FREUDE,² J. LEUTHOLD,⁴ C. KOOS,^{1,2,6} AND M. KOHL^{1,*}

¹Institute of Microstructure Technology (IMT), Karlsruhe Institute of Technology (KIT), Karlsruhe, Germany

²Institute of Photonics and Quantum Electronics (IPQ), Karlsruhe Institute of Technology (KIT), Karlsruhe, Germany

³Institute of Nanotechnology (INT), Karlsruhe Institute of Technology (KIT), Karlsruhe, Germany

⁴Institute of Electromagnetic Fields (IEF), ETH Zurich, Zurich, Switzerland

⁵e-mail: sascha.muehlbrandt@kit.edu

⁶e-mail: christian.koos@kit.edu

*Corresponding author: manfred.kohl@kit.edu

Received 21 March 2016; revised 31 May 2016; accepted 1 June 2016 (Doc. ID 261635); published 7 July 2016

Silicon-plasmonics enables the fabrication of active photonic circuits in CMOS technology with unprecedented operation speed and integration density. Regarding applications in chip-level optical interconnects, fast and efficient plasmonic photodetectors with ultrasmall footprints are of special interest. A particularly promising approach to silicon-plasmonic photodetection is based on internal photoemission (IPE), which exploits intrinsic absorption in plasmonic waveguides at the metal–dielectric interface. However, while IPE plasmonic photodetectors have already been demonstrated, their performance is still far below that of conventional high-speed photodiodes. In this paper, we demonstrate a novel class of IPE devices with performance parameters comparable to those of state-of-the-art photodiodes while maintaining footprints below $1 \mu\text{m}^2$. The structures are based on asymmetric metal–semiconductor–metal waveguides with a width of less than 75 nm. We measure record-high sensitivities of up to 0.12 A/W at a wavelength of 1550 nm. The detectors exhibit opto-electronic bandwidths of at least 40 GHz. We demonstrate reception of on–off keying data at rates of 40 Gbit/s. © 2016 Optical Society of America

OCIS codes: (040.0040) Detectors; (250.5403) Plasmonics; (040.5160) Photodetectors; (160.1890) Detector materials; (310.6628) Subwavelength structures, nanostructures.

<http://dx.doi.org/10.1364/OPTICA.3.000741>

1. INTRODUCTION

Chip-level optical interconnects are key to overcoming communication bottlenecks in high-performance computing systems [1]. To achieve high data rates and energy-efficient operation, the corresponding transmitters and receivers must be seamlessly co-integrated with CMOS electronics. This is currently impeded by the vastly different footprints of electronic and photonic components: whereas state-of-the-art field effect transistors can be fabricated [2] with a half-pitch of less than 14 nm, typical dimensions of photonic devices amount to tens or even hundreds of micrometers. Plasmonics enables a large reduction of these dimensions by exploiting charge-density oscillations that are strongly confined to metal–dielectric or metal–semiconductor (MS) interfaces [3], thereby leading to short carrier transit times and ultrasmall device capacitances. In combination with the large conductivities of metals, any RC limits are hence shifted to very high frequencies, which leads to unprecedented operation speeds [4]. At the transmitter side, ultracompact plasmonic modulators operating at data rates of 40 Gbit/s and beyond have been demonstrated recently [5,6]. For the receiver, however, miniaturized

plasmonic photodetectors with technically relevant performance still remain to be shown. Previous demonstrations cover photodetectors that exploit passive plasmonic nanostructures for concentrating the incident light to an ultra-small area of an absorbing semiconductor such as germanium [7,8]. In these approaches, measured sensitivities (responsivities) are typically less than 0.001 A/W due to the limited efficiencies and the intrinsic absorption losses of plasmonic light concentrators. In an alternative approach, the intrinsic absorption of metal can be directly used for photodetection. This is accomplished by internal photoemission (IPE), which exploits photon-assisted transmission of hot carriers across a potential barrier at MS interfaces [9,10]. Propagation of surface plasmon polaritons (SPPs) in plasmonic waveguides is ideally suited for realizing such devices, as the plasmonic mode is strongly localized at the MS interface and, hence, perfectly concentrates the light to the region where absorption leads to the highest generation rate of photo-electrons. The potential of IPE has been demonstrated in several different plasmonic devices, including resonant plasmonic antennas or nanocavities [11–13] and metal-coated silicon waveguides [14–17].

However, the sensitivity of IPE-based photodetectors has so far been limited by the width of the potential barrier that optically excited hot carriers need to overcome. Highest reported sensitivities amount to only 0.019 A/W at a wavelength of 1550 nm [16]—more than 1 order of magnitude below those of state-of-the-art waveguide-integrated germanium PIN or avalanche photodiodes [18–20]. Moreover, the bandwidths of these devices are limited to 7 GHz by relatively long drift regions of more than 2 μm .

In this paper we introduce and experimentally demonstrate a novel approach to exploiting internal photoemission for photo-detection. For brevity, we name the resulting device a PIPED, an acronym for plasmonic internal photoemission detector. Our PIPED combines record-high sensitivities of more than 0.12 A/W at 1550 nm with large optoelectronic bandwidths well above 40 GHz. We prove the viability of this concept by receiving on–off keying (OOK) data at a rate of 40 Gbit/s. To the best of our knowledge, this is the first demonstration of data transmission at technically relevant bit rates using plasmonic IPE detectors. This superior performance is due to a nanoscale silicon drift region of only 75 nm width, sandwiched between two metal layers with distinctively different light absorption characteristics and Schottky barrier heights. This leads to an ultranarrow potential barrier and to short transit times under the influence of an external bias voltage. Further simulations and measurements imply that with an optimized coupling approach the sensitivities can be increased at least by a factor of 2.

2. OPERATION PRINCIPLE

The energy band diagram of the Au–Si–Ti photodetector junction is sketched in Fig. 1. The junction forms a metal–semiconductor–metal (MSM) light waveguide that guides SPPs along the z direction, which is perpendicular to the drawing plane of Fig. 1. The silicon core has nanoscale dimensions of the order of $w = 100$ nm and constitutes a potential barrier between the metals, thus impeding any charge transfer. The silicon core is weakly p-doped with an acceptor concentration of $n_A \approx 10^{15}$ cm^{-3} . The SPPs dissipate their energy mainly at the Si–Ti interface, because titanium has a larger magnitude of the imaginary part of the complex permittivity $\epsilon = \epsilon_1 - j\epsilon_2$ than gold at a wavelength of $\lambda = 1550$ nm ($\epsilon_{\text{Ti}} = 1.6 - j30.56$ [21], $\epsilon_{\text{Au}} = -112.7 - j6.85$ [22]). The SPP absorption length along the z coordinate is below 1 μm (see Fig. S1 in Supplement 1), so the junction length is not truly important and can be chosen in the range $L = (1 \dots 20)$ μm , depending on the requirements for the dark current. The absorbed plasmonic wave with angular frequency ω creates hot electrons in the metal within a few nanometers from the interface. The maximum carrier energies exceed the Fermi energy by ω [Fig. 1(a)]. These hot electrons have an increased probability of crossing the potential barrier at the metal–semiconductor interface either by thermionic emission or by tunneling, where the tunneling probability depends on the height of the potential barrier and on its width at a given carrier energy [23]. This process is known as internal photoemission [10]. The barrier heights are assumed to be $\Phi_{\text{Au}} = 0.82$ eV [24] and $\Phi_{\text{Ti}} = 0.62$ eV [25] for the Au–Si and the Si–Ti interfaces, respectively. This establishes a built-in potential difference across the silicon core of about $\varphi_{\text{bi}} = 0.2$ V in thermal equilibrium [Fig. 1(a)]. Without external bias, φ_{bi} impedes electron photoemission from the highly absorbing titanium into the silicon layer, and no significant current flow can be measured. A positive

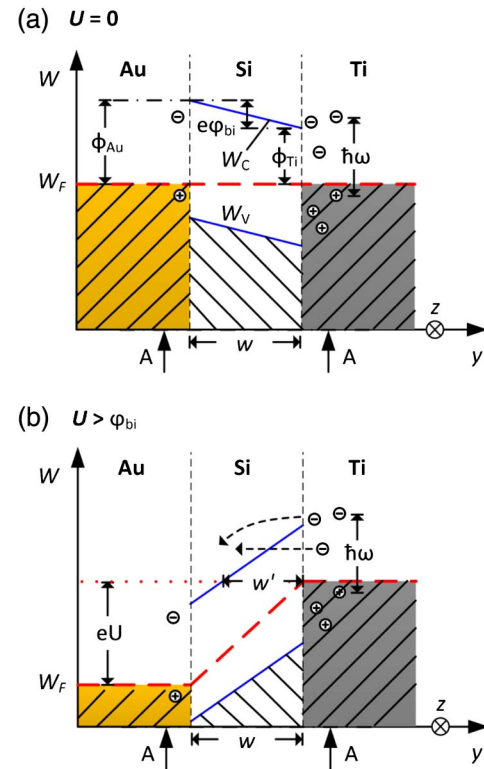


Fig. 1. Energy band diagram of an Au–Si–Ti junction. Energy W , lateral direction y as in Fig. 2(b). The silicon layer of width w constitutes a potential-barrier-impeding charge transfer between the metals. The energy of the Schottky barrier heights are Φ_{Au} and Φ_{Ti} . W_C denotes the silicon conduction band edge, and W_V is the valence band edge. The junction is capable of guiding light in the form of SPPs, which are absorbed mainly at the Si–Ti interface. Absorbed SPPs create hot electrons with a maximum energy of ω above the Fermi energy W_F . (a) Thermal equilibrium, no bias voltage. The built-in potential φ_{bi} leads to a constant negative electric field along the y axis inside the silicon layer. Hot carriers created by light absorption at the Si–Ti interface are impeded to cross the barrier by the built-in field. (b) Nonequilibrium under applied forward bias voltage U , counted positive in the direction Au \rightarrow Ti. The voltage drops across the silicon layer. For $U > \varphi_{\text{bi}}$, the barrier width w is reduced to an effective width w' , thereby increasing the emission probability across the barrier. The section A–A corresponds to associated sections in the device schematics of Fig. 2.

potential exceeding $U = \varphi_{\text{bi}}$ is required at the gold electrode to enable photoemission from the titanium layer, which is on zero potential [see Fig. 1(b)]. The silicon layer is much smaller than the depletion layer width of either MS interface due to the weak doping [26]. Hence, the external voltage dominates the voltage drop across the silicon layer for large bias, and a constant electric field is present, indicated by a linear increase of the conduction and the valence band energies W_C and W_V along y . The effective barrier width w' at the Si–Ti interface is consequently reduced, and thus the transmission probability of hot electrons is increased. For a silicon core width of $w = 75$ nm and an applied voltage of $U = 3$ V (or $U = 1$ V), the effective barrier width for electrons at the Fermi level in titanium is reduced to $w' = 17$ nm (or $w' = 58$ nm). The effective barrier width for hot electrons is even smaller and progressively decreases to zero for increasing electron energies, leading to a much larger sensitivity than measured with other IPE-based photodetectors.

Furthermore, the large electric field inside the silicon enables high drift velocities. The device structure of the detector is sketched in Figs. 2(a) and 2(b). Near-infrared light is launched from a silicon photonic strip waveguide into the SPP waveguide junction. The silicon is tapered down from a width of 400 nm in the photonic waveguide to a width of $w = (75...200)$ nm at the MSM junction. The tapered section has a length of $0.55 \mu\text{m}$ and converts the photonic mode to a plasmonic mode [27]. The silicon core of the detector is wider at its base than at its top as a consequence of the fabrication process. A SiO_2 hard mask used for etching the silicon core and a metal top cover are not removed after fabrication. The metal thicknesses on either side of the MSM waveguide are $t = 40$ nm. As an example, Figs. 2(c) and 2(d) show devices with $w = 200$ nm and a device length of $L = 1 \mu\text{m}$. Thus, the active parts of the device consume less than $1 \mu\text{m}^2$ of chip area.

To assess the limitations of the operating speed, we consider several effects: The hot-electron lifetime in metals [28] is only a few hundred femtoseconds, which defines the time interval in which transitions from the metal to the semiconductor can occur. The carrier drift time through a 75 nm thick semiconductor layer takes only about 750 fs, assuming a saturation drift velocity [26] of 10^7 cm/s. Similarly, the capacitance of the MSM junction can be estimated based on an equivalent parallel-plate capacitor C across the semiconductor region. With a metal height of 275 nm, a device length of $L = 5 \mu\text{m}$, and a silicon width of $w = 75$ nm, a capacitance below $C = 2$ fF is obtained. This value does not

take into account the capacitance of the contact pads. Based on this, an RC time constant of only 100 fs can be estimated by assuming a resistor with $R = 50 \Omega$ in the bias circuit, as depicted in Fig. 2(a). Hence, all these estimates lead to bandwidths of at least several hundred gigahertz, indicating that compact IPE-based detectors have the potential to overcome the existing speed limitations of conventional photodetectors.

3. DETECTOR FABRICATION

The fabrication of asymmetric MSM junctions with a silicon width below 100 nm is challenging, because a short circuit between the electrodes must be avoided. We use electron-beam lithography and isotropic silicon etching with SF_6 to create the silicon core. Details of the fabrication process are given in Supplement 1; see Fig. S2 there. As a first step, a hard mask is structured by using thermally oxidized silicon. By masking and etching, the SiO_2 is removed outside the plasmonic section, leaving a “tabletop” structure above. The silicon sidewalls are selectively metallized by directional evaporation virtually normal to the sidewalls. During metallization, the hard mask prevents a short circuit (see Supplement 1 for details), and silicon widths of 75 nm become feasible. For testing, we fabricate a set of silicon-on-insulator (SOI) chips with different Au–Si–Ti junctions, establishing various PIPEDs with lengths of $L = (1...20) \mu\text{m}$ and silicon core widths of $w = (75...200)$ nm.

4. PIPED CHARACTERIZATION

In the following, we report on the results obtained from four different PIPEDs, which we denote PIPED #1...#4. An overview of the physical device properties and the measured performance parameters is given in Table 1. For the sample design and in the fabrication process we covered a large region of the parameter space, and we optimized the devices for various design goals: The ultranarrow detector cores of PIPEDs #1 and #2 were used to demonstrate the high responsivities and the linearity of the device. PIPED #3 is most suitable for polarization contrast measurements, as both polarizations couple with a similar efficiency to the core for this detector width (see Section 4). PIPED #4 exhibits the longest carrier drift length and hence was used to demonstrate the high opto-electronic bandwidth, even for the worst case of a large device. Not all experiments could be done with all devices, as they were driven to their limits and partially damaged during the experiments by applying high bias voltages, or they deteriorated by oxidation of the (not yet protected) titanium.

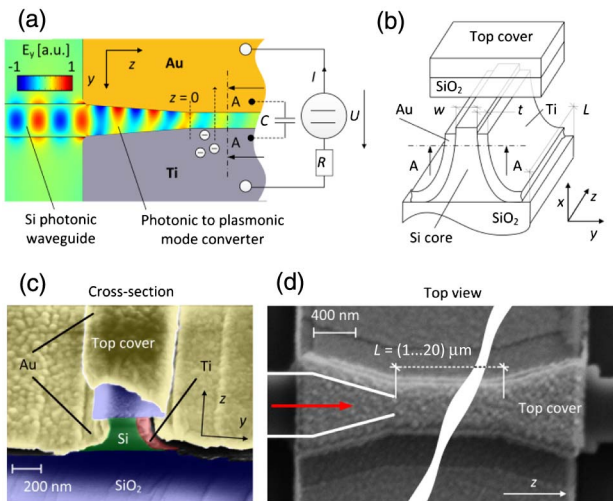


Fig. 2. Detector structure and operation principle. (a) Light is coupled from a silicon photonic waveguide to the Au–Si–Ti junction, which is biased with the external voltage U . Absorbed SPPs generate hot electrons, which are transferred between the adjacent metals. The section A–A indicates the regions in which the band diagrams in Fig. 1 are drawn. (b) Schematic of the detector junction with length L . The silicon core is sandwiched between two metal layers (Au, Ti) of thickness t . The silicon core has a height of 300 nm and is wider at the base than at the top as a consequence of the fabrication process. The core width at the top is denoted as w . The SiO_2 hard mask on top of the silicon and its gold cover result from the fabrication process and are shown only in the back half of the structure. (c) Cleaved facet of fabricated Au–Si–Ti junction. Due to cleaving, the gold cover on the thermally grown SiO_2 hard mask has partially detached. (d) Top view of a plasmonic detector. The red arrow denotes the light propagation direction. The Au–Si–Ti junction is hidden below the hard mask and the top metallization.

Table 1. Properties of PIPED Samples #1–#4 (N.A.: Not Available)

	Width w	Length L	Sensitivity S (1550 nm)	Band-Width	Data Exp.
#1	75 nm	5 μm	0.019 A/W (1 V) 0.043 A/W (2 V) 0.126 A/W (3.25 V)	N.A.	N.A.
#2	75 nm	5 μm	0.042 A/W (1 V) 0.102 A/W (2 V)	N.A.	40 Gbit/s (1 V)
#3	150 nm	4 μm	0.014 A/W (1 V) 0.027 A/W (2 V)	N.A.	N.A.
#4	200 nm	20 μm	N. A.	>40 GHz	N.A.

Oxidation can be inhibited by coating the samples with an oxygen-blocking layer [29].

The diffraction gratings we used for light coupling excited the photonic waveguide mode with a dominantly horizontal electric field component (see Section 3 in Supplement 1). The total current through the device I comprises a dark current I_d depending only on the bias voltage U , and a photocurrent I_p . The photocurrent increases linearly with the incident optical power P , and the sensitivity $S = I_p/P$ depends on the applied voltage such that $I_p = S(U)P$, which is in contrast to conventional PIN photodiodes. Dark current I_d and photocurrent I_p of PIPED #1 ($w = 75$ nm, $L = 5$ μm) are characterized at a wavelength of 1550 nm. The total current $I = I_p + I_d$ is measured as a function of laser power P and external DC-bias voltage U (positive polarity from gold to titanium). Figure 3(a) shows the mean of two subsequently measured $I - U$ characteristics of a detector without and with illumination at a power of $P = 310$ μW . Both the gold and the titanium electrodes are capable of charge carrier emission into the silicon core. Depending on the sign

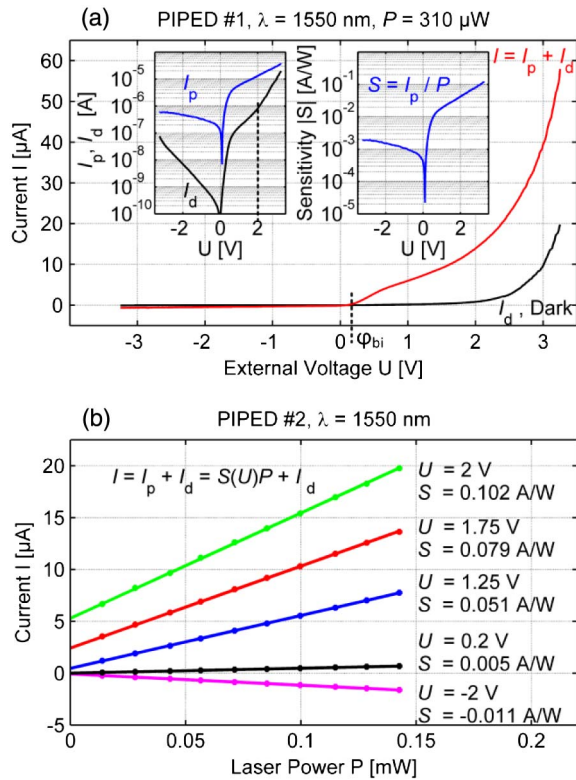


Fig. 3. Photodetector DC characterization for PIPEDs #1 and #2 ($L = 5$ μm and width $w = 75$ nm). (a) Total current I for an incident laser power of $P = 310$ μW and dark current I_d as a function of the external (bias) voltage U . For voltages $U > \phi_{\text{bi}}$, the photocurrent is positive, corresponding to carrier injection from the titanium. The photocurrent grows exponentially beyond $U = 1$ V. The insets show a semi-logarithmic plot of dark and photocurrent, as well as the corresponding sensitivity $S = I_p/P$, exceeding $S > 0.12$ A/W^{-1} for a bias voltage of $U = 3.25$ V. The dashed line in the left inset separates the dark current into regions of different exponential growth. As this particular behavior is not present in the photocurrent, we exclude the presence of avalanche multiplication. (b) Total device current I versus laser power P for various bias voltages. The laser power P is measured at the input of the photonic-to-plasmonic mode converter. The filled circles denote the measurements; the solid lines represent linear fits to the measured data.

of the bias voltage U , the resulting current can be positive or negative. As expected, the magnitude of the photocurrent is significantly larger for a positive bias $U > \phi_{\text{bi}}$, which facilitates photoemission across the small potential barrier for electrons generated at the highly absorbing Si–Ti interface. The left-hand side inset of Fig. 3(a) shows a semi-logarithmic display of photocurrent I_p and dark current I_d , and the inset to the right displays the sensitivity S . For $U > 1$ V, the sensitivity increases exponentially with increasing bias voltage. No saturation is observable. In particular, a positive photocurrent of $I_p = 38$ μA is measured for an optical input power of 310 μW and a bias voltage of $U = 3.25$ V. This corresponds to a sensitivity of $S = 0.12$ A/W , which is more than a factor of 6 higher than the sensitivity of other IPE-based photodetectors [13,16]. Furthermore, the sensitivity is of the same order of magnitude as values typically measured for comparable state-of-the-art waveguide-based SiGe devices [18–20]. The steep increase of $S = I_p/P$ for bias voltages $\phi_{\text{bi}} < U < 1$ V is caused by the fact that the transmission probability of electrons across the Ti–Si interface is sensitive to the distinct shape of the potential barrier. A detailed quantitative model is the subject of ongoing investigations. Figure 3(b) shows the total current $I = I_p + I_d = S(U)P + I_d$ as a function of the optical input power for the element PIPED #2 ($w = 75$ nm, $L = 5$ μm). The parameter is the bias voltage. The linear increase of current with optical power indicates that the measured photocurrent is due to internal photoemission [9] and not to two-photon absorption in silicon [30].

To examine the influence of carrier multiplication by the impact ionization in silicon, we consider the dominant ionization coefficient α_i for electrons. For the maximum bias $U = 3$ V (or at $U = 1$ V), the electric field strength is $E = U/w = 3$ V/75 nm = 40 V/ μm (or $E = 1$ V/75 nm = 13 V/ μm). The corresponding electron ionization coefficient in silicon amounts to $\alpha_i = 3$ μm^{-1} (or $\alpha_i = 10^{-3}$ μm^{-1}) [26]. This leads to ionization probabilities of $\alpha_i w = 0.23$ (or $\alpha_i w = 0.075$) inside the silicon core. The resulting avalanche multiplication factor $M_0 = \exp(\alpha_i w) = 1.25$ (or $M_0 = 1.08$) is only slightly larger than 1, which shows that avalanche multiplication cannot contribute significantly. This finding is supported by comparing photocurrent I_p to dark current I_d [see left inset of Fig. 3(a)]. The logarithmic plot of the photocurrent is essentially a straight line for bias voltages 1 V $< U < 3.25$ V, while the dark current characteristic has two distinct slopes in the regions 1 V $< U < 2$ V and 2 V $< U < 3.25$ V. This cannot be explained with avalanche multiplication, which acts alike on thermally generated carriers and on photogenerated carriers. Note that the current–voltage characteristics do not follow conventional formulas for MSM-type devices due to the narrow width of the junctions. A detailed quantitative model is the subject of ongoing investigations.

5. OPTICAL COUPLING AND PHOTOCURRENT POLARIZATION DEPENDENCE

The coupling of optical fields to plasmonic MSM-type waveguides is strongly polarization dependent [3]. Hence, the photocurrent is expected to show a strong contrast between situations in which optical fields that have dominantly vertical or dominantly horizontal electric field components are absorbed. Only horizontally polarized optical fields can couple to a pure MSM junction

with vertical metallic side walls. To explore the polarization dependence of the photocurrent, we cleaved an SOI chip with PIPED #3 ($w = 150$ nm) and accessed the photonic waveguides from the chip edges using polarization maintaining fibers. The slow polarization axis of the fiber is aligned with the surface normal of the photonic chip. The orientation of the linear polarization coupled into the polarization maintaining (PM) fiber is then controlled with a half-wave plate; see Supplement 1 for experimental details. The half-wave plate is rotated, corresponding to a full 360° revolution of the incoming electric field vector. The linear polarization state at the fiber input is characterized by an angle Θ between the polarization direction and the slow axis of the PM fiber. Figure 4(a) shows the photocurrent, which is measured as a function of this angle Θ . Note that, due to the strong birefringence of the PM fiber, only the photocurrents at polarization angles of $\Theta = 90^\circ \times n$, with $n = 0, 1, 2, \dots$, belong to linear polarization states at the chip input, whereas unknown elliptical polarization states are obtained for any other Θ . Angles of $\Theta_v = 0^\circ, 180^\circ$ correspond to a dominant vertical electric field component E_y , and angles of $\Theta_h = 90^\circ, 270^\circ$ correspond to a dominant horizontal electric field component E_x . The photocurrents I_v for vertical electric field alignments at angles Θ_v are nearly 2 times larger than the currents I_h for horizontal electric field alignments at angles Θ_h . This is surprising at first sight, and needs a detailed investigation of the optical coupling for either polarization. To this end, we use a three-dimensional finite-element method and simulate the coupling of the photonic waveguide modes (dominant E_x or dominant E_y) to the plasmonic photodetector. Figures 4(b) and 4(c) show cross sections of the normalized electric fields in the x - y plane at the input of the silicon core of width $w = 150$ nm, directly at the interface between the core and the tapered mode converter, denoted as $z = 0$ in Fig. 2(a). The optical coupling efficiencies $\eta_{v,h}$ of the dominantly vertically or dominantly horizontally polarized fields are given by referring the power at the input of the silicon core ($z = 0$) to the total power P_0 propagating in the photonic waveguide. These coupling efficiencies $\eta_v = 0.57$ and $\eta_h = 0.50$ are essentially similar for this detector width, and, hence, the influence of light absorption in the mode converter on the photocurrent polarization contrast can be neglected. However, the field distributions for both polarizations differ considerably. Figure 4(b) shows that the dominantly horizontally polarized photonic input field couples mainly to the Au–Si–Ti junction, and that the field is concentrated inside the silicon core between the two metals. In contrast to that, the dominantly vertically polarized photonic input field cannot couple to the Au–Si–Ti junction, as such a mode is not supported by the MSM plasmonic waveguide. However, the junction has a SiO_2 hard mask and a gold top cover, which are residuals from fabrication [see Figs. 2(c) and 2(d)]. This layer sequence constitutes an MS interface that supports an SPP mode that couples well to the vertically polarized field of the photonic waveguide. This plasmonic mode confines the electric field to the SiO_2 hard mask.

The light absorption in the metals depends on the respective optical field overlap and the imaginary part of the permittivity. The local absorption is in proportion to $\text{Im}(\epsilon) \times |E|^2$. While the optical power concentrates on the side of the gold, the field penetration is so small (due to the high conductivity of gold) that absorption as compared to the absorption in titanium is negligible, even if the field strength at the titanium side is small.

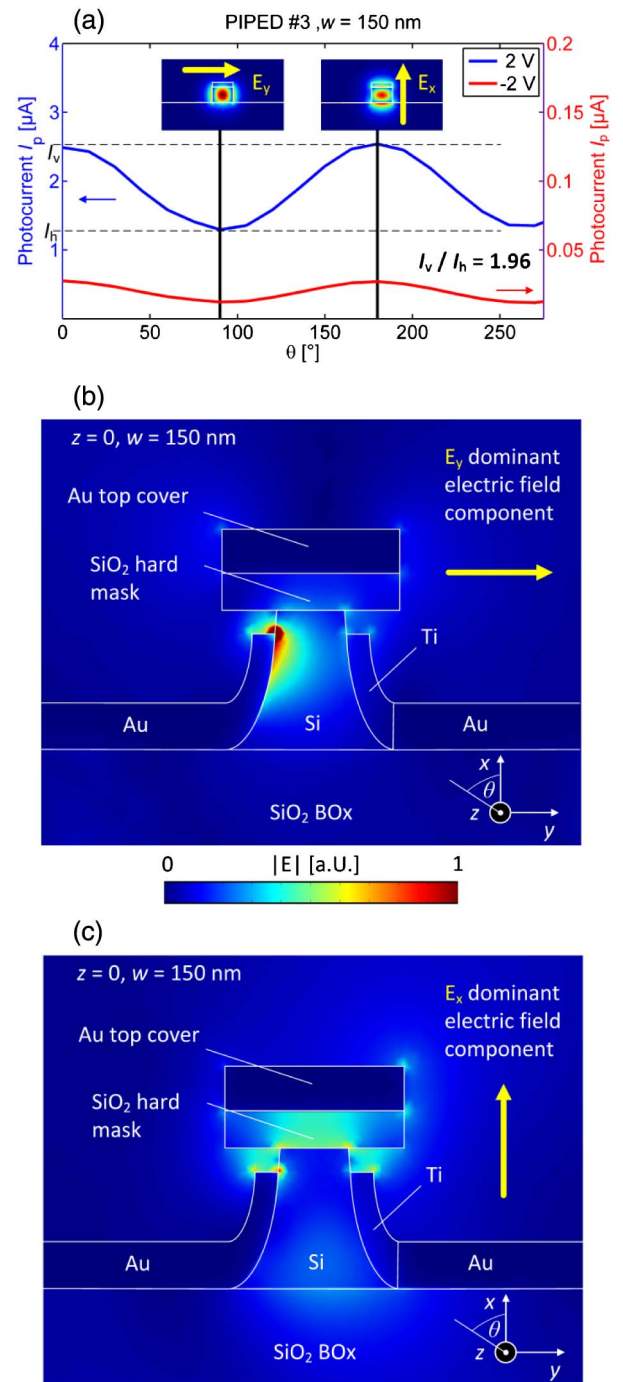


Fig. 4. Polarization dependence of photocurrent and simulation of optical fields for PIPED #3 with $w = 150$ nm. (a) Photocurrent I_p as a function of angle Θ between the direction of the linear polarization at the fiber input and the slow axis of the PM fiber with forward bias (blue) and reverse bias (red). The surface normal of the photonic chip is aligned in parallel to the slow axis of the PM fiber. The angles $\Theta_v = 0^\circ, 180^\circ, 360^\circ$ correspond to a dominant vertical electric field component E_y , and $\Theta_h = 90^\circ, 270^\circ$ correspond to a dominant horizontal electric field component E_x . The insets illustrate the respective electric fields in the photonic waveguide. (b) Electric field magnitude at the input of the silicon core, indicated by $z = 0$ in Fig. 2(a), after coupling from a photonic mode with a dominantly horizontal electric field component. The light is localized in the silicon core. (c) Electric field magnitude at the input of the silicon core ($z = 0$) after coupling from a photonic mode with a dominantly vertical electric field component. Light is localized in the SiO_2 hard mask. Both field distributions deposit the optical power efficiently in the titanium; see Table 2.

Table 2. Fraction of Absorbed Optical Power in the Photonic-to-Plasmonic Mode Converter (conv.), in the Detector Core, and Total Absorbed Power Per Metal Contact Relative to the Total Optical Input Power P_0

Core Width 150 nm	Power Absorbed in the Au Contact/ P_0			Power Absorbed in the Ti Contact/ P_0		
	Conv.	Core	Tot.	Conv.	Core	Tot.
Dominant horizontal polarization	0.073	0.056	0.13	0.38	0.42	0.80
Dominant vertical polarization	0.018	0.022	0.04	0.40	0.43	0.83

Table 2 gives an overview of the absorbed power fraction inside the mode converter and inside the detector core for each input polarization. The absorption in the titanium is 8 times larger than in the gold for both polarizations, even for a relatively wide silicon layer width of $w = 150$ nm. The vertically polarized plasmonic mode deposits even slightly more optical power in the titanium as compared to the horizontally polarized mode, for which the structure was designed. In this case, the absorption occurs mostly at the apex of the metallic side walls, where the potential barrier is thinnest and, hence, the photocurrent is largest.

From our measurements we infer that the PIPED sensitivity can be doubled by choosing the proper polarization. For our best sample, PIPED #1, we would hence expect an increase of sensitivity from 0.12 to 0.24 A/W. The currently employed mode converter consumes a significant fraction of the input power but cannot contribute significantly to the photocurrent due to the large separation of the metals compared to the detector core. If the photonic-to-plasmonic converter is redesigned for the specific polarization requirements and for a smaller absorption, even more power would reach the silicon core and hence be absorbed at the Si-Ti interface, such that the sensitivity could be further improved.

6. OPTO-ELECTRONIC BANDWIDTH AND DATA RECEPTION EXPERIMENTS

We experimentally quantify the electrical bandwidth of PIPEDs using a two-port vector network analyzer (VNA). The VNA stimulus is amplified and drives a LiNbO₃ Mach-Zehnder modulator, generating intensity-modulated optical signals up to 65 GHz. A calibrated photodetector (Anritsu MN4765 A) with a known opto-electronic transfer function is used as a reference. The output pads of the PIPED are contacted with standard RF probes (PicoProbe 40A-GS-100-P). The measured PIPED transfer function (including the RF probe characteristic) is normalized to the value at the lowest modulation frequency of 40 MHz and displayed as a relative sensitivity in Fig. 5(a). Due to bandwidth limitations of modulator and amplifiers, the PIPED current exhibits strong noise for frequencies larger than 40 GHz. Nevertheless, the calibrated transfer function is flat throughout the measured range. Hence, we expect that the RF bandwidth of the device is significantly larger than 40 GHz. The transfer function exhibits dips at approximately 4, 7, and 30 GHz, which are attributed to imperfect connectors of the RF probes.

Investigated detector #4 is $L = 20$ μm long and $w = 200$ nm wide. All other devices have smaller dimensions and are expected to show even larger bandwidths. This is confirmed by additional measurements, where we observe comparably flat transfer functions for devices of various lengths and widths. This implies that the devices are neither transit-time limited nor RC limited.

We expect that the PIPED exhibits this large opto-electronic bandwidth for both input polarizations. The polarization with dominant vertical field alignment creates hot carriers preferentially at the apex of the titanium layer, where the drift distance of the photoelectrons is the shortest. The bandwidth should be slightly higher for this mode in comparison to the mode with horizontal field alignment. However, this has no significant impact on the investigated operating frequency range.

To demonstrate the viability of our photodetector as a receiver of optical data, we perform a data transmission experiment. We generate an OOK optical signal with a 40 Gbit/s pseudo-random bit sequence (PRBS) having a pattern length of $2^{31} - 1$. The signal is received with photodetector PIPED #2. We use an available RF amplifier with 50 Ω instead of a transimpedance amplifier, which would be employed in real-world applications. Figure 5(b) shows the eye diagram at 40 Gbit/s. We use an optical input power of $P = 1.6$ mW and a bias voltage of $U = 1$ V at which the dark current is not too large in comparison to the photocurrent so that the electrical signal-to-noise power ratio remains

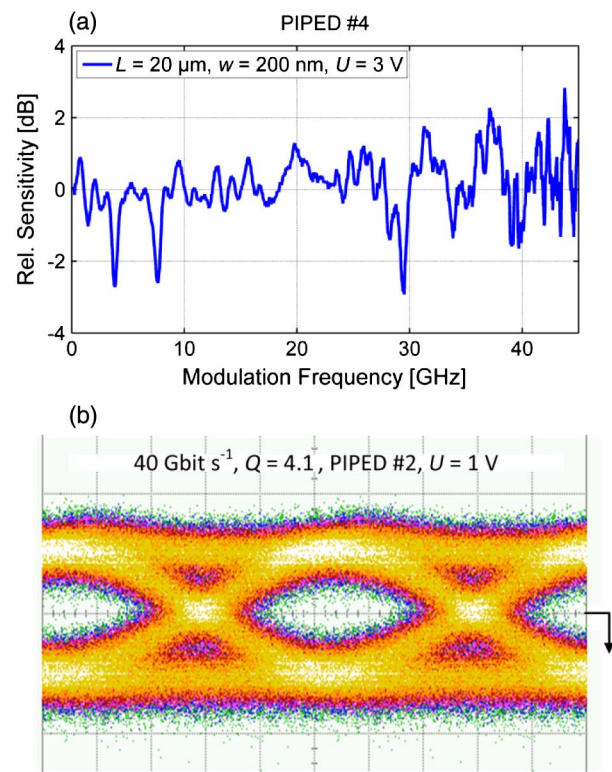


Fig. 5. Frequency-dependent photodetector sensitivity and data reception experiment. (a) Electro-optic transfer function of sensitivity, normalized to the sensitivity at 40 MHz. The dips at 4, 7, and 30 GHz originate from reflections at the RF probe. The measurement has been done with the longest and widest device, PIPED #4. (b) Eye diagram measured with PIPED #2 for OOK at 40 Gbit/s with a measured quality factor of $Q = 4.1$ and an estimated BER of 2×10^{-5} . The bias voltage is $U = 1$ V, and the optical power at the input of the detector is $P = 1.6$ mW. The DC part of the device current has been removed.

sufficiently large. The DC part has been subtracted. We measure a quality factor of $Q = 4.1$, corresponding to a bit error ratio [31] (BER) of 2×10^{-5} . This BER is well below the threshold for a standard second-generation forward-error correction [32] with 7% overhead.

7. CONCLUSION

In summary, we demonstrate a high-speed and high-sensitivity internal photoemission plasmonic photodetector (PIPED) with a sensitivity exceeding 0.12 A/W at 1550 nm. By changing the state of polarization, the sensitivity can be doubled. We succeeded in data reception of bit rates up to 40 Gbit/s using a PIPED receiver with a core footprint of $5 \mu\text{m} \times 155 \text{ nm}$, and with a total footprint of less than $1 \mu\text{m}^2$. Our experimental findings represent record results for plasmonic photodetectors based on IPE. We believe that compact IPE-based detectors have the potential to overcome the existing speed limitations of presently available photodetectors. As such, they could become key components of future high-speed optical transmission systems.

Funding. European Commission (NAVOLCHI); European Research Council (ERC) “EnTeraPIC” (280145); Helmholtz International Research School of Teratronics (HIRST); Alfried Krupp von Bohlen und Halbach-Stiftung; Karlsruhe Nano Micro Facility (KNMF), a Helmholtz Research Infrastructure at Karlsruhe Institute of Technology (KIT).

See Supplement 1 for supporting content.

REFERENCES

1. D. A. B. Miller, “Device requirements for optical interconnects to silicon chips,” *Proc. IEEE* **97**, 1166–1185 (2009).
2. M. Bohr, “14 nm process technology: opening new horizons” (2014), <http://www.intel.com/content/dam/www/public/us/en/documents/pdf/foundry/mark-bohr-2014-idf-presentation.pdf>, retrieved March 15, 2016.
3. S. A. Maier, *Plasmonics: Fundamentals and Applications* (Springer, 2007).
4. S. S. Mousavi, A. Stöhr, and P. Berini, “Plasmonic photodetector with terahertz electrical bandwidth,” *Appl. Phys. Lett.* **104**, 143112 (2014).
5. A. Melikyan, L. Alloatti, A. Muslija, D. Hillerkuss, P. C. Schindler, J. Li, R. Palmer, D. Korn, S. Muehlbrandt, D. van Thourhout, B. Chen, R. Dinu, M. Sommer, C. Koos, M. Kohl, W. Freude, and J. Leuthold, “High-speed plasmonic phase modulators,” *Nat. Photonics* **8**, 229–233 (2014).
6. C. Haffner, W. Heni, Y. Fedoryshyn, J. Niegemann, A. Melikyan, D. L. Elder, B. Baeuerle, Y. Salamin, A. Josten, U. Koch, C. Hoessbacher, F. Ducry, L. Juchli, A. Emboras, D. Hillerkuss, M. Kohl, L. R. Dalton, C. Hafner, and J. Leuthold, “All-plasmonic Mach-Zehnder modulator enabling optical high-speed communication at the microscale,” *Nat. Photonics* **9**, 525–528 (2015).
7. L. Tang, S. E. Kocabas, S. Latif, A. K. Okyay, D.-S. Ly-Gagnon, K. C. Saraswat, and D. A. B. Miller, “Nanometre-scale germanium photodetector enhanced by a near-infrared dipole antenna,” *Nat. Photonics* **2**, 226–229 (2008).
8. T. Ishi, J. Fujikata, K. Makita, T. Baba, and K. Ohashi, “Si nanophotodiode with a surface plasmon antenna,” *Jpn. J. Appl. Phys.* **44**, L364–L366 (2005).
9. R. H. Fowler, “The analysis of photoelectric sensitivity curves for clean metals at various temperatures,” *Phys. Rev.* **38**, 45–56 (1931).
10. J. S. Helman and F. Sánchez-Sinencio, “Theory of internal photoemission,” *Phys. Rev. B* **7**, 3702–3706 (1973).
11. M. W. Knight, H. Sobhani, P. Nordlander, and N. J. Halas, “Photodetection with active optical antennas,” *Science* **332**, 702–704 (2011).
12. K.-T. Lin, H.-L. Chen, Y.-S. Lai, and C.-C. Yu, “Silicon-based broadband antenna for high responsivity and polarization-insensitive photo-detection at telecommunication wavelengths,” *Nat. Commun.* **5**, 3288 (2014).
13. B. Desiatov, I. Goykhman, N. Mazurski, J. Shappir, J. B. Khurgin, and U. Levy, “Plasmonic enhanced silicon pyramids for internal photoemission Schottky detectors in the near-infrared regime,” *Optica* **2**, 335–338 (2015).
14. A. Akbari, R. N. Tait, and P. Berini, “Surface plasmon waveguide Schottky detector,” *Opt. Express* **18**, 8505–8514 (2010).
15. M. Casalino, M. Iodice, L. Sirteto, I. Rendina, and G. Coppola, “Asymmetric MSM sub-bandgap all-silicon photodetector with low dark current,” *Opt. Express* **21**, 28072–28082 (2013).
16. S. Zhu, G. Q. Lo, and D. L. Kwong, “Low-cost and high-speed SOI waveguide-based silicide Schottky-barrier MSM photodetectors for broadband optical communications,” *IEEE Photon. Technol. Lett.* **20**, 1396–1398 (2008).
17. I. Goykhman, B. Desiatov, J. Khurgin, J. Shappir, and U. Levy, “Locally oxidized silicon surface-plasmon Schottky detector for telecom regime,” *Nano Lett.* **11**, 2219–2224 (2011).
18. C.-K. Tseng, W.-T. Chen, K.-H. Chen, H.-D. Liu, Y. Kang, N. Na, and M.-C. M. Lee, “A self-assembled microbonded germanium/silicon heterojunction photodiode for 25 Gb/s high-speed optical interconnects,” *Sci. Rep.* **3**, 3225 (2013).
19. L. Vivien, L. Viro, D. Marris-Morini, J.-M. Hartmann, P. Crozat, E. Cassan, C. Baudot, F. Boeuf, and J.-M. Fédéli, “40 Gbit/s germanium waveguide photodiode,” in *Optical Fiber Communication Conference/National Fiber Optic Engineers Conference*, OSA Technical Digest (online) (Optical Society of America, 2013), paper OM2J.3.
20. S. Assefa, F. Xia, and Y. A. Vlasov, “Reinventing germanium avalanche photodetector for nanophotonic on-chip optical interconnects,” *Nature* **464**, 80–84 (2010).
21. M. A. Ordal, R. J. Bell, R. W. Alexander, L. A. Newquist, and M. R. Querry, “Optical properties of Al, Fe, Ti, Ta, W, and Mo at submillimeter wavelengths,” *Appl. Opt.* **27**, 1203–1209 (1988).
22. R. L. Olmon, B. Slovick, T. W. Johnson, D. Shelton, S.-H. Oh, G. D. Boreman, and M. B. Raschke, “Optical dielectric function of gold,” *Phys. Rev. B* **86**, 235147 (2012).
23. R. H. Fowler and L. Nordheim, “Electron emission in intense electric fields,” *Proc. R. Soc. London Ser. A* **119**, 173–181 (1928).
24. T. P. Chen, T. C. Lee, C. C. Ling, C. D. Beling, and S. Fung, “Current transport and its effect on the determination of the Schottky-barrier height in a typical system: gold on silicon,” *Solid-State Electron.* **36**, 949–954 (1993).
25. A. M. Cowley, “Titanium-silicon Schottky barrier diodes,” *Solid-State Electron.* **13**, 403–414 (1970).
26. S. M. Sze, *Physics of Semiconductor Devices* (Wiley, 1981).
27. D. F. P. Pile and D. K. Gramotnev, “Adiabatic and nonadiabatic nanofocusing of plasmons by tapered gap plasmon waveguides,” *Appl. Phys. Lett.* **89**, 041111 (2006).
28. H. Petek and S. Ogawa, “Femtosecond time-resolved two-photon photoemission studies of electron dynamics in metals,” *Prog. Surf. Sci.* **56**, 239–310 (1997).
29. J.-M. Jeong, M. S. Oh, B. J. Kim, C.-H. Choi, B. Lee, C.-S. Lee, and S. G. Im, “Reliable synthesis of monodisperse microparticles: prevention of oxygen diffusion and organic solvents using conformal polymeric coating onto poly (dimethylsiloxane) micromold,” *Langmuir* **29**, 3474–3481 (2013).
30. R. W. Boyd, “Optically induced damage and multiphoton absorption,” in *Nonlinear Optics*, 3rd ed. (Academic, 2008), Chap. 12, pp. 543–560.
31. W. Freude, R. Schmogrow, B. Nebendahl, M. Winter, A. Josten, D. Hillerkuss, S. Koenig, J. Meyer, M. Dreschmann, M. Huebner, C. Koos, J. Becker, and J. Leuthold, “Quality metrics for optical signals: eye diagram, Q-factor, OSNR, EVM and BER,” in *14th International Conference on Transparent Optical Networks (ICTON)* (IEEE, 2012).
32. Z. Xuezhong, P. Koka, M. O. McCracken, H. Schwetman, J. G. Mitchell, Y. Jin, R. Ho, K. Raj, and A. V. Krishnamoorthy, “Energy-efficient error control for tightly coupled systems using silicon photonic interconnects,” *J. Opt. Commun. Netw.* **3**, A21–A31 (2011).